

On the fluid-structure interaction of a flexible cantilever cylinder at low Reynolds numbers

Shayan Heydari,^{1,*} Neelesh A. Patankar,² Mitra J. Z. Hartmann,² and Rajeev K. Jaiman^{1,†}

¹*Department of Mechanical Engineering, The University of British Columbia, Vancouver, BC Canada V6T 1Z4*

²*Department of Mechanical Engineering, Northwestern University,
2145 Sheridan Road, Evanston, Illinois 60208, USA*

(Dated: May 26, 2021)

We present a numerical study to investigate the fluid-structure interaction of a flexible circular cantilever cylinder in a uniform cross-flow. We employ a fully-coupled fluid-structure solver based on the three-dimensional Navier-Stokes equations and the Euler-Bernoulli beam theory. We examine the dynamics of the cylinder for a wide range of reduced velocities (U^*), mass ratios (m^*), and Reynolds numbers (Re). Of particular interest is to explore the possibility of flow-induced vibrations in a slender cantilever cylinder of aspect ratio $AR = 100$ at laminar subcritical Re regime (i.e., no periodic vortex shedding). We assess the extent to which such a flexible cylindrical beam can sustain flow-induced vibrations and characterize the contribution of the beam's flexibility to the stability of the wake at low Re . We show that when certain conditions are satisfied, the flexible cantilever cylinder undergoes sustained large-amplitude vibrations. The frequency of the oscillations is found to match the frequency of the periodic fluid forces for a particular range of system parameters. In this range, the frequency of the transverse vibrations is shown to match the first-mode natural frequency of the cylinder, indicating the existence of the lock-in phenomenon. The range of the lock-in regime is shown to have a strong dependence on Re and m^* . We discover that unlike the steady wake behind a stationary rigid cylinder, the wake of a low mass ratio flexible cantilever cylinder could lose its stability in the lock-in regime at Reynolds numbers as low as $Re = 22$. A combined VIV-galloping type instability is shown to be the possible cause of the wake instability at this Re regime. These findings attempt to generalize our understanding of the flow-induced vibrations in flexible cantilever structures and can have a profound impact on the development of novel flow-measurement sensors.

I. INTRODUCTION

Flow-induced vibrations (FIVs) have significant consequences and are essential to predict in numerous fields, such as marine/offshore, civil, biomedical, and aerospace engineering. Considerable research has been done in recent decades to characterize the underlying mechanism and explore the practical aspects of flow-induced vibrations in a wide range of domains, including vibration control [1–3], energy harvesting [4–8], and sensing [9, 10]. The phenomenon of flow-induced vibration in bluff bodies has received special attention in the literature due to complex vortex dynamics and nonlinear physics involved in the interaction of a bluff body and fluid flow. In this regard, the flow-induced vibration of an elastically-mounted rigid cylinder has served as a prototypical model for both experimental and numerical studies [11]. It has been shown that asymmetric vortex shedding from the wake of an elastically-mounted rigid cylinder exerts unsteady transverse loads that could lead to sustained large-amplitude vibrations called vortex-induced vibrations (VIVs) [12]. VIVs are characterized by a frequency match between the frequency of the periodic vortex shedding and the vibration frequency of the cylinder [12, 13]. When the natural frequency of the cylinder is close to the

vortex shedding frequency, the VIV phenomenon results in a complex evolution of the shedding frequency, which deviates from the Strouhal frequency of its stationary counterpart. In this frequency regime, the vortex formation locks on to the natural frequency of the structure, which in turn creates a strong coupling between the cylinder and fluid flow [12]. Several studies have shown that the peak vibration amplitude of an elastically-mounted rigid cylinder, with only one degree-of-freedom in the transverse direction, is approximately $O(D)$ [14], where D denotes the cylinder diameter. The magnitude of the peak vibration amplitude is known to be a function of fluid and structural parameters, such as Reynolds number and mass-damping ratio [15], and has been shown to have a slightly higher value for a two-degree-of-freedom cylinder [16]. Comprehensive reviews regarding the VIV of elastically-mounted rigid cylinders could be found in Refs. [14, 15, 17–19].

More recently, studies have focused on the dynamic response of flexible slender structures at high Reynolds numbers [20–22] to give new physical insight into the phenomenon of vortex-induced vibrations. Due to the complex interaction of nonlinear wake dynamics with numerous flexible modes, the VIV modeling and prediction poses serious challenges for long flexible structures. For example, studies on thin risers have found that ocean currents excite several vibration modes and frequencies along the span of a riser during VIVs [23–25]. In a short-term perspective, VIV effects can lead to drag amplification and large dynamic bending stresses. These large-

* Corresponding author. Email address: sheydari@mail.ubc.ca

† Email address: rjaiman@mech.ubc.ca

amplitude vibrations lead to fatigue failure in slender structures and marine risers in the long term if not controlled properly [26]. An Experimental study on the VIV of a flexible cantilever cylinder in the laminar flow regime has found some distinct differences between the dynamics of a flexible cantilever cylinder and a flexible riser in the VIV regime. A flexible pinned-pinned beam, such as a marine riser, has been shown to vibrate at monotonically increasing frequencies with each eigenmode gradually growing in modal weight as the reduced velocity is increased [27]. However, for a flexible cantilever cylinder, although higher modes are observed at higher reduced velocities, the cylinder has been shown to oscillate with only one vibration eigenmode during VIVs [28]. In line with the works done in the field of vortex-induced vibrations, in our current work, we examine the dynamic response of a flexible cantilever cylinder at low Reynolds numbers to give new insight into the topic of flow-induced vibrations in flexible slender structures.

Our interest in studying the dynamics of a flexible cantilever cylinder at low Reynolds numbers originates from the intriguing problem of sensing through whiskers in some mammals, such as rats and seals. Experimental studies on the mechanical response of isolated rat vibrissae (whiskers) to low-speed airflow have revealed that air currents of magnitude 0.5 to 5.6 m/s, typically found in natural environments, generate significant vibrissal motion that carries information about the direction and magnitude of the airflow [29, 30]. More interestingly, behavioral experiments have shown that rats use the information from their whiskers to localize airflow sources [31]. To characterize the geometry of a rat's tapered conical whisker, two parameters, namely arc length S and base diameter D_b , are defined. Typically, in a rat's mystacial pad, the ratio of a whisker's arc length S to base diameter D_b is between $100 < S/D_b < 400$ and the wind speeds translate into Reynolds numbers < 50 , based on D_b of the whisker [29].

In addition to rats, harbor seals, for example, have been shown to use their highly sensitive undulated whiskers to sense hydrodynamic information of water flows and detect fluid structures without auditory or visual cues [32]. An experimental study on a model of a seal whisker has shown that a whisker in the wake of a stationary rigid cylinder undergoes large-amplitude oscillations, with the frequency of the oscillations being close to the shedding frequency of the upstream wake [33]. These oscillations are known to help seals detect upstream wakes and estimate the size and shape of the wake-generating body [33].

Although considerable research has been done to understand the problem of sensing through whiskers, there have been limited studies on the mechanism behind the dynamics of whiskers in fluid flow. In particular, the oscillatory response of a whisker at laminar subcritical Reynolds numbers, i.e., $Re < Re_{cr} \approx 45$ [34, 35], is not well understood. In our current work, we investigate fluid-structure interaction of a flexible cantilever cylin-

der, as a simplified model of a whisker, to help answer two specific questions: (i) can we observe sustained vibrations in the flexible cantilever cylinder at subcritical Re with laminar wake flow, and (ii) what is the relationship between the cylinder dynamics and stability of the wake at this Re regime? Understanding the underlying fluid-structure dynamics of a flexible cantilever cylinder, inspired by the dynamics of whiskers, is of vital importance for developing novel flow-measurement sensors [9] and brings us one step closer towards a complete mapping of the sensing properties of whiskers.

The key non-dimensional parameters involved in the fluid-structure interaction of the flexible cantilever cylinder are mass ratio m^* , Reynolds number Re , and reduced velocity U^* defined as

$$m^* = \frac{4m}{\pi D^2 \rho^f}, \quad Re = \frac{\rho^f U_0 D}{\mu^f}, \quad U^* = \frac{U_0}{f_n D}, \quad (1)$$

where m is the mass per unit length of the cylinder, D is the cylinder diameter, ρ^f and μ^f are the density and dynamic viscosity of the fluid, respectively, U_0 is the magnitude of the uniform flow velocity, and f_n is the natural frequency of the first mode of vibration. The non-dimensional parameters studied in our current work are within $20 \leq Re \leq 40$, $U^* \in [2, 19]$ and $1 \leq m^* \leq 1000$, which cover a practical range of values in the laminar subcritical Re regime.

A schematic of the flexible cantilever cylinder is given in Fig. 1. The cylinder is connected to a fixed support at $z = 0$. The Young's modulus and second moment of area of the cylinder are denoted by E and I , respectively. As shown in Fig. 1, due to fluid forces acting on the cylinder, it initially deforms in the streamwise direction. Also, depending on the system parameters, the cylinder could exhibit an unsteady dynamic response, resulting in periodic vortex shedding patterns in the wake region. A systematic analysis of the dynamic response of the cylinder is conducted in our current work, where we use high-fidelity

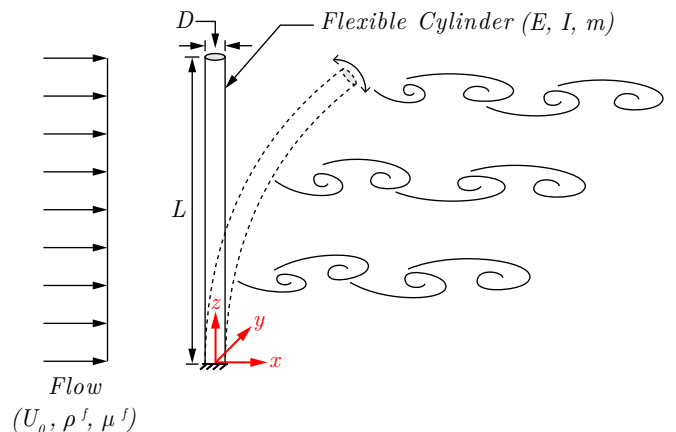


FIG. 1: Schematic of a flexible cantilever cylinder of diameter D and length L interacting with a uniform flow of velocity U_0 .

numerical simulations to examine the fluid-structure interaction of the cylinder for a broad range of system parameters.

The content of the paper is structured as follows. The governing equations for modeling the cylinder dynamics and the coupling strategy between the fluid and structural solvers are discussed in Section II. In addition, we provide the results for the grid convergence study at the end of this section. In section III we cover the results of our study and discuss the dynamic response characteristics of the cylinder in detail. Finally, we finish the paper with a conclusion in section IV.

II. NUMERICAL METHODOLOGY

This section presents a three-dimensional numerical framework for studying the fluid-structure interaction of the flexible cantilever cylinder with an incompressible viscous flow. To model the coupled dynamics of the cylinder, we employ a three-dimensional computational domain as shown in Fig. 2. The cylinder is placed at an offset distance of $15D$ and $45D$ from the inflow and outflow surfaces, respectively. Fixed structural support is imposed at one end of the cylinder ($z = 0$), and the no-slip boundary condition is applied at the fluid-structure interface Γ^{fs} . The size of the computational domain is $60D \times 30D \times L$ where a uniform velocity of $\mathbf{u}^f = (U_0, 0, 0)$ with a magnitude of U_0 in the x-direction is given at the inflow surface. The slip boundary condition is applied to the side surfaces $\Gamma_{\text{side-1}}^f$ and $\Gamma_{\text{side-2}}^f$, and the traction-free boundary condition, given by $\boldsymbol{\sigma}^f \cdot \mathbf{n}^f = 0$, is specified at the outflow surface.

In the following, we discuss the governing equations for modeling the dynamics of the flexible cantilever cylinder and present the strategy implemented to couple the fluid and structural solvers.

A. Governing equations

We consider the three-dimensional incompressible Navier-Stokes equations coupled with the Euler-Bernoulli beam theory to examine the coupled dynamics of the flexible cantilever cylinder. We formulate the governing equation for the Euler-Bernoulli beam in a Lagrangian reference frame and take a body-fitted moving boundary approach based on the arbitrary Lagrangian-Eulerian (ALE) description [36] to formulate the unsteady Navier-Stokes equations for the viscous incompressible fluid. The body-fitted treatment of the fluid-structure interface through the ALE description of the flow field provides accurate modeling of the boundary layer over the deformable surface of the structure.

1. Navier-Stokes equations for a moving-boundary problem

The unsteady Navier-Stokes equations for a viscous incompressible fluid flow in an arbitrary Lagrangian-Eulerian reference frame on the fluid domain $\Omega^f(t)$ are

$$\rho^f \frac{\partial \mathbf{u}^f}{\partial t} \Big|_{\hat{\mathbf{x}}^f} + \rho^f (\mathbf{u}^f - \mathbf{u}^m) \cdot \nabla \mathbf{u}^f = \nabla \cdot \boldsymbol{\sigma}^f + \mathbf{b}^f \quad \text{on } \Omega^f(t), \quad (2)$$

$$\nabla \cdot \mathbf{u}^f = 0 \quad \text{on } \Omega^f(t), \quad (3)$$

where $\mathbf{u}^f = \mathbf{u}^f(\mathbf{x}^f, t)$ and $\mathbf{u}^m = \mathbf{u}^m(\mathbf{x}^f, t)$ denote the fluid and mesh velocities defined for each spatial point $\mathbf{x}^f \in \Omega^f(t)$ respectively, \mathbf{b}^f is the body force applied to the fluid and $\boldsymbol{\sigma}^f$ is the Cauchy stress tensor for a Newtonian fluid, given as

$$\boldsymbol{\sigma}^f = -p\mathbf{I} + \mu^f (\nabla \mathbf{u}^f + (\nabla \mathbf{u}^f)^T), \quad (4)$$

where p denotes the fluid pressure, and μ^f is the dynamic viscosity of the fluid. The first term in Eq. (2) represents the partial derivative of \mathbf{u}^f with respect to time while the ALE referential coordinate $\hat{\mathbf{x}}^f$ is kept fixed.

The fluid forcing acting on the beam's surface is calculated by integrating the surface traction at the first layer of the elements located on the fluid-structure interface. The instantaneous coefficients of lift and drag forces are quantified as

$$C_L = \frac{1}{\frac{1}{2}\rho^f U_0^2 DL} \int_{\Gamma^{\text{fs}}} (\boldsymbol{\sigma}^f \cdot \mathbf{n}) \cdot \mathbf{n}_y d\Gamma, \quad (5)$$

$$C_D = \frac{1}{\frac{1}{2}\rho^f U_0^2 DL} \int_{\Gamma^{\text{fs}}} (\boldsymbol{\sigma}^f \cdot \mathbf{n}) \cdot \mathbf{n}_x d\Gamma, \quad (6)$$

where \mathbf{n}_x and \mathbf{n}_y are the Cartesian components of the unit outward normal vector \mathbf{n} . In the next section, we present the equation for modeling the structural dynamics of the flexible cantilever cylinder using the Euler-Bernoulli beam theory.

2. Euler-Bernoulli beam theory for a flexible structure

We consider the flexible cantilever cylinder as a slender structure with relatively small lateral motions. Therefore, the Euler Bernoulli beam theory can be applied to model its dynamic response. Let Ω^s be the structural domain consisting of structure coordinates $\mathbf{x}^s = (x, y, z)$. We solve the transverse displacements $\mathbf{w}^s(z, t)$ using the Euler-Bernoulli beam equation excited by the distributed unsteady fluid force per unit length \mathbf{f}^s . The motion of the flexible cantilever cylinder is governed by the fluid forces and involves integrating pressure and shear stress effects on the cylinder surface. Neglecting the damping and shear effects, we take the equation of motion for the flexible cantilever cylinder as:

$$m \frac{\partial^2 \mathbf{w}^s(z, t)}{\partial t^2} + EI \frac{\partial^4 \mathbf{w}^s(z, t)}{\partial z^4} = \mathbf{f}^s(z, t), \quad (7)$$

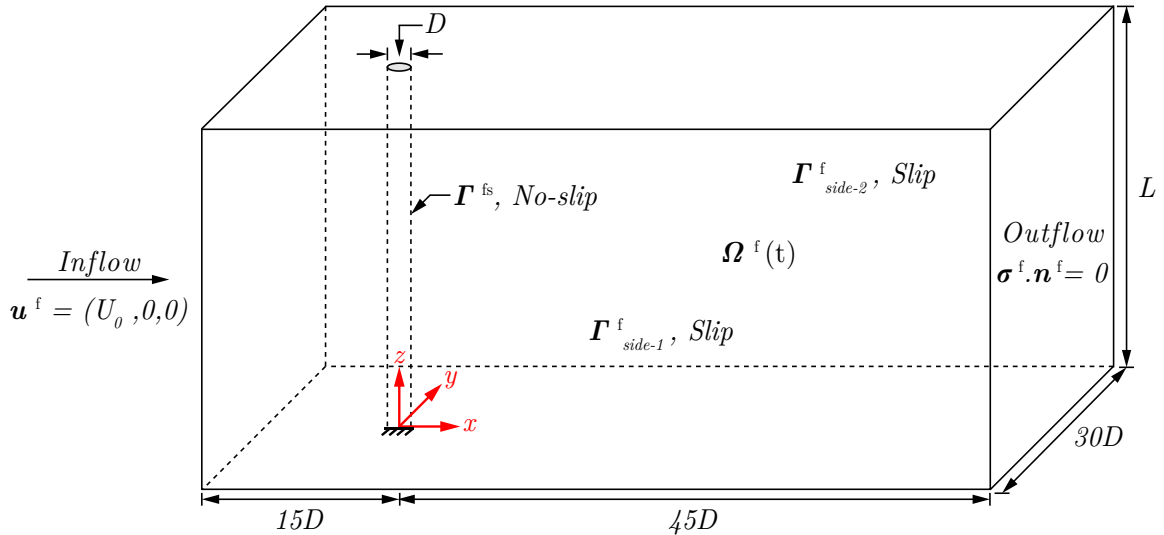


FIG. 2: Schematic of the computational domain with details of the boundary conditions.

where $m = \rho^s A$ is the mass per unit length of the cylinder, with A being the cross-sectional area of the cylinder. Under the cantilever (clamped-free) configuration, the boundary conditions at the clamped end of the cylinder are given as:

$$\mathbf{w}^s(z, t)|_{z=0} = 0, \quad \left. \frac{\partial \mathbf{w}^s(z, t)}{\partial z} \right|_{z=0} = 0. \quad (8)$$

To solve Eq. (7), we consider a mode superposition approach for the dynamic response of the cylinder. The n^{th} mode natural frequency of the flexible cantilever cylinder is given by

$$f_n = \frac{\lambda_n^2}{2\pi L^2} \sqrt{\frac{EI}{m + m_a}}, \quad (9)$$

where n is the mode number, m_a is the added mass of the fluid per unit length defined as $m_a = \pi D^2 \rho^f / 4$ and λ_n is the dimensionless frequency parameter for the n^{th} mode of vibration. The λ_n values are given in Table I. The modal parameters are based on the values reported in Ref. [37] for flexible cantilever beams of constant cross section.

The cylinder motion is solved using simple linear vibration analysis. The displacements from the mean position

TABLE I: Modal parameters for flexible cantilever beams of constant cross section [37].

Mode number, n	λ_n	σ_n
1	1.87510407	0.734095514
2	4.69409113	1.018467319
3	7.85475744	0.999224497
4	10.99554073	1.000033553
5	14.13716839	≈ 1
≥ 6	$(2n-1)\pi/2$	≈ 1

of the cylinder are assumed to be small and characterized based on the normal modes of the vibration found using an eigenvalue analysis. The mode shapes of the cantilever cylinder are taken as the sums of sine, cosine, sinh, and cosh functions of $\lambda_n z / L$ written as:

$$S^n(z) = \cosh\left(\frac{\lambda_n z}{L}\right) - \cos\left(\frac{\lambda_n z}{L}\right) - \sigma_n \sinh\left(\frac{\lambda_n z}{L}\right) + \sigma_n \sin\left(\frac{\lambda_n z}{L}\right), \quad (10)$$

where S^n denotes the mode shape associated with the n^{th} mode of vibration and σ_n is the non-dimensional parameter dependent on the mode number (see Table I for σ_n values).

3. Treatment of the fluid-structure interface

We need to satisfy the continuity of velocity and traction at the fluid-structure interface. Let $\Gamma^{\text{fs}} = \partial\Omega^f(0) \cap \partial\Omega^s$ be the fluid-structure interface at $t = 0$ and $\Gamma^{\text{fs}}(t) = \boldsymbol{\varphi}^s(\Gamma^{\text{fs}}, t)$ be the interface at time t . The required conditions to be satisfied are as follows:

$$\mathbf{u}^f(\boldsymbol{\varphi}^s(\mathbf{x}_0^s, t), t) = \mathbf{u}^s(\mathbf{x}_0^s, t), \quad (11)$$

$$\int_{\boldsymbol{\varphi}^s(\gamma, t)} \boldsymbol{\sigma}^f(\mathbf{x}^f, t) \cdot \mathbf{n} d\Gamma(\mathbf{x}^f) + \int_{\gamma} \mathbf{t}^s d\Gamma = 0, \quad (12)$$

where $\boldsymbol{\varphi}^s$ denotes the position vector that maps the initial position \mathbf{x}_0^s of the flexible cantilever cylinder to its position at time t , i.e., $\boldsymbol{\varphi}^s(\mathbf{x}^s, t) = \mathbf{x}_0^s + \mathbf{w}^s(\mathbf{x}^s, t)$, \mathbf{t}^s is the fluid traction vector relating to the fluid forcing as $\mathbf{f}^s(z, t) = \int_{\Gamma^{\text{fs}}} \mathbf{t}^s d\Gamma$, and \mathbf{u}^s is the velocity of the structure at time t given by $\mathbf{u}^s = \partial\boldsymbol{\varphi}^s/\partial t$. Here, \mathbf{n} is the outer normal to the fluid-structure interface, γ is any part of the interface Γ^{fs} in the reference configuration, $d\Gamma$ is the

differential surface area and $\varphi^s(\gamma, t)$ is the corresponding fluid part at time t . The above conditions are satisfied such that the fluid velocity is exactly equal to the velocity of the structure at the fluid-structure interface.

To couple the fluid and structure equations, we use a nonlinear partitioned iterative approach based on the nonlinear iterative force correction (NIFC) scheme described in [38, 39]. At each time step, the fluid traction applied to the surface of the cylinder is projected onto the eigenvectors to find the values of the generalized modal forces. The projected modal forces are then used to determine the modal amplitudes and displacements for the next time step.

To account for the changes in the cylinder geometry, we explicitly control the motion of each mesh node while satisfying the kinematic consistency of the discretized interface. The movement of the internal finite element nodes is chosen such that the mesh quality does not deteriorate as the displacements of the cylinder become large. For this purpose, we assume the fluid mesh to represent a hyperelastic solid model. In addition, a standard Lagrangian finite element technique is used to adapt the mesh to the new geometry of the domain.

B. Grid convergence study

The coupled dynamics of the flexible cantilever cylinder is examined through a numerical framework that has been verified and validated extensively for FSI problems in an earlier study [24]. Thus, we proceed with the grid convergence study here. We discretize the computational domain into unstructured hexahedral finite element grids with a boundary layer mesh around the flexible cantilever cylinder.

We start with a relatively coarse grid denoted by M1 and successively increase the number of elements by approximately a factor of 2 to achieve the M2 and M3 meshes. An isometric view of the discretized domain and a z -plane slice of the unstructured grid for the M2 mesh is given in Fig. 3.

For the grid convergence study, we have examined the dynamics of the cylinder at $Re = 40$, $m^* = 1$, and $U^* = 11$. Grid convergence errors are calculated by taking the finest mesh, M3, as the reference case. The values of the frequency ratio (f_y/f_n), mean streamwise deformation ($\overline{A_x}/D$), root-mean-square (rms) of the dimensionless transverse vibration amplitude (A_y^{rms}/D), and the force coefficients ($\overline{C_D}$ and C_L^{rms}) are given in Table II.

According to Table II, the relative errors using the M2 mesh are less than 2%; therefore, the M2 mesh is chosen as the suitable grid for our present study. The results mentioned in Table II are for a computational domain with 16 layers in the spanwise direction. After doing an independent grid convergence study on the number of spanwise layers, ranging from 8 to 64, we found that 16 layers are adequate to capture the essential three-dimensional features of the fluid-structure system.

III. RESULTS AND DISCUSSION

In this section, we present our results for the fluid-structure interaction of the flexible cantilever cylinder for $20 \leq Re \leq 40$, $U^* \in [2, 19]$ and $1 \leq m^* \leq 1000$. In addition, we discuss the wake dynamics for the range of studied parameters. Finally, we relate our findings to real-world observations regarding the oscillatory motion of whiskers in laminar fluid flow.

A. Response characteristics

We first present the response characteristics of the flexible cantilever cylinder at $m^* = 1$ for $20 \leq Re \leq 40$ and $U^* \in [2, 19]$. The root-mean-square (rms) values of the dimensionless transverse vibration amplitude A_y^{rms}/D at the tip of the cylinder ($z/L = 1$) is given in Fig. 4. We find that at $Re = 20$, the cylinder remains in its steady deflected position, i.e., $A_y^{rms} = 0$, within the range of studied U^* . This steady response is also observed at $Re = 22$ for $U^* \leq 6$ and at $24 \leq Re \leq 40$ for $U^* \leq 5$ (see Fig. 4). However, there is a particular range of U^* within which the cylinder is shown to undergo sustained vibrations for $22 \leq Re \leq 40$. We observe that the peak of the transverse vibration amplitude in this range is within $U^* \in [7, 8]$. As shown in Fig. 4, at $Re = 22$, the peak of the A_y^{rms}/D is at $U^* = 8$ with a magnitude of approximately 0.18. However, at higher Re , the peak of the vibration amplitude shifts to $U^* = 7$, where the oscillations are shown to grow in magnitude as Re is increased. For instance, the peak of the A_y^{rms}/D has a magnitude of approximately 0.26 at $Re = 24$, whereas at $Re = 40$, the maximum A_y^{rms}/D is approximately equal to 0.49. We find that at $Re = 40$, the cylinder experiences sustained oscillations for reduced velocities between $U^* \in [6, 19]$; however, for lower Re , the oscillations are present for a narrower range of U^* . A more broadband oscillatory response with respect to U^* at higher Re is due to larger inertial fluid forces that overcome the viscous damping.

Fig. 5a demonstrates the time histories of the transverse vibration amplitude calculated from the mean deformed position of the cylinder $(A_y - \overline{A_y})/D$ at $z/L = 1$ and lift coefficient C_L at $Re = 40$, $m^* = 1$, and $U^* = 7$. We observe that the transverse vibrations at the tip of the cylinder are in-phase with the variations of the lift coefficient. In addition, we show that the peak of the dimensionless transverse vibration frequency (f_y/f_n) matches the peak of the dimensionless lift coefficient frequency (f_{C_L}/f_n) in the frequency domain at $f_y/f_n = f_{C_L}/f_n = 1$ (see Fig. 5b). This frequency match indicates that the lock-in phenomenon is driving the oscillations at $U^* = 7$.

To specify the range of the lock-in regime, we have provided the variations of the dimensionless transverse vibration frequency f_y/f_n and lift coefficient frequency f_{C_L}/f_n at $m^* = 1$ for $Re = 22, 30$ and 40 with respect to U^* in Fig. 6. We show that at $Re = 22$, f_y/f_n and

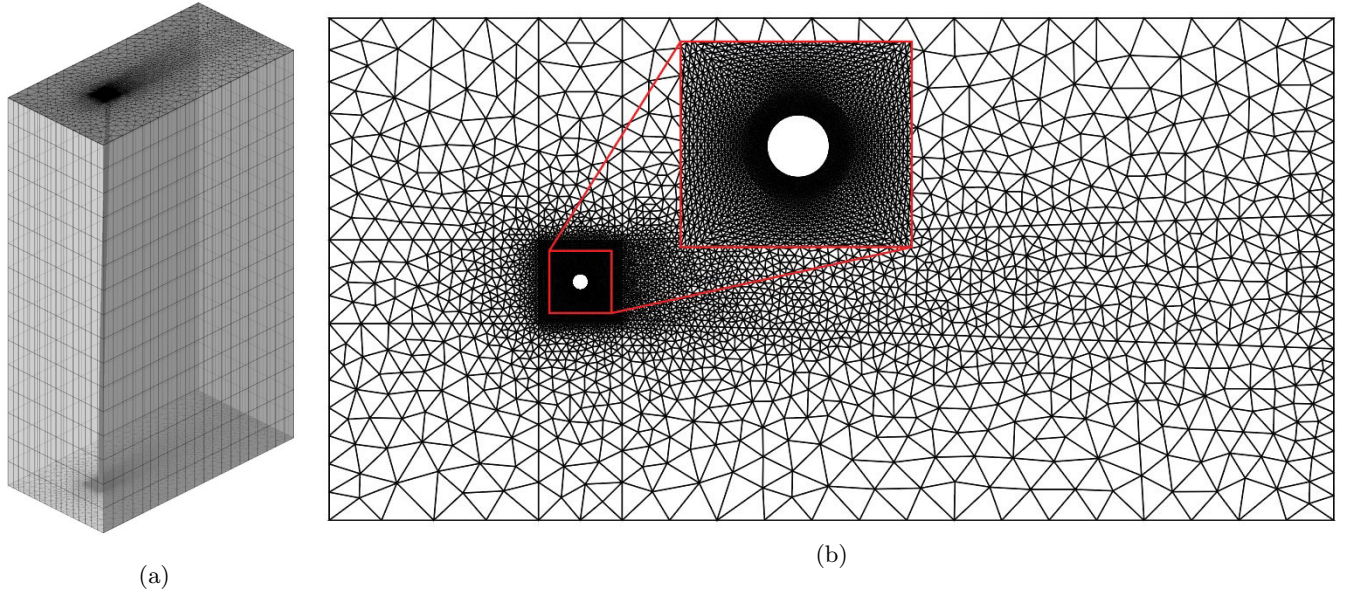


FIG. 3: Computational finite element grid for the M2 mesh: (a) isometric view of the discretized computational domain; (b) representative z -plane slice of the unstructured grid with a closeup view of the boundary layer mesh.

TABLE II: Grid convergence study results for the flexible cantilever cylinder interacting with a uniform cross-flow at $Re = 40$, $m^* = 1$, and $U^* = 11$.

	M1	M2	M3
Number of nodes	142290	285396	564672
Number of elements	271458	547470	1086591
Time-step size Δt	0.001	0.001	0.001
Frequency ratio f_y/f_n	1.2522	1.2522	1.2522
Mean streamwise deformation $\overline{A_x}/D$	2.6000 (0.26%)	2.5966 (0.13%)	2.5933
rms of transverse vibration amplitude A_y^{rms}/D	0.3188 (1.98%)	0.3134 (0.25%)	0.3126
Mean drag coefficient $\overline{C_D}$	1.6958 (0.37%)	1.6917 (0.13%)	1.6895
rms of lift coefficient C_L^{rms}	0.0197 (14.53%)	0.0175 (1.74%)	0.0172

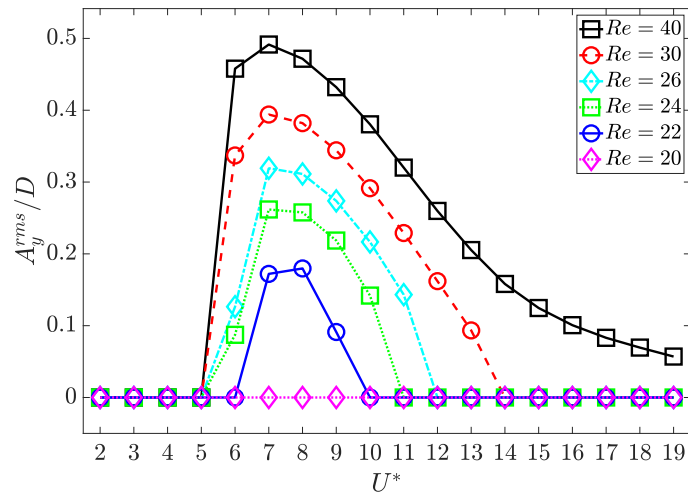


FIG. 4: Root-mean-square (rms) value of the dimensionless transverse vibration amplitude A_y^{rms}/D at $z/L = 1$ as a function of U^* at $m^* = 1$ for $20 \leq Re \leq 40$.

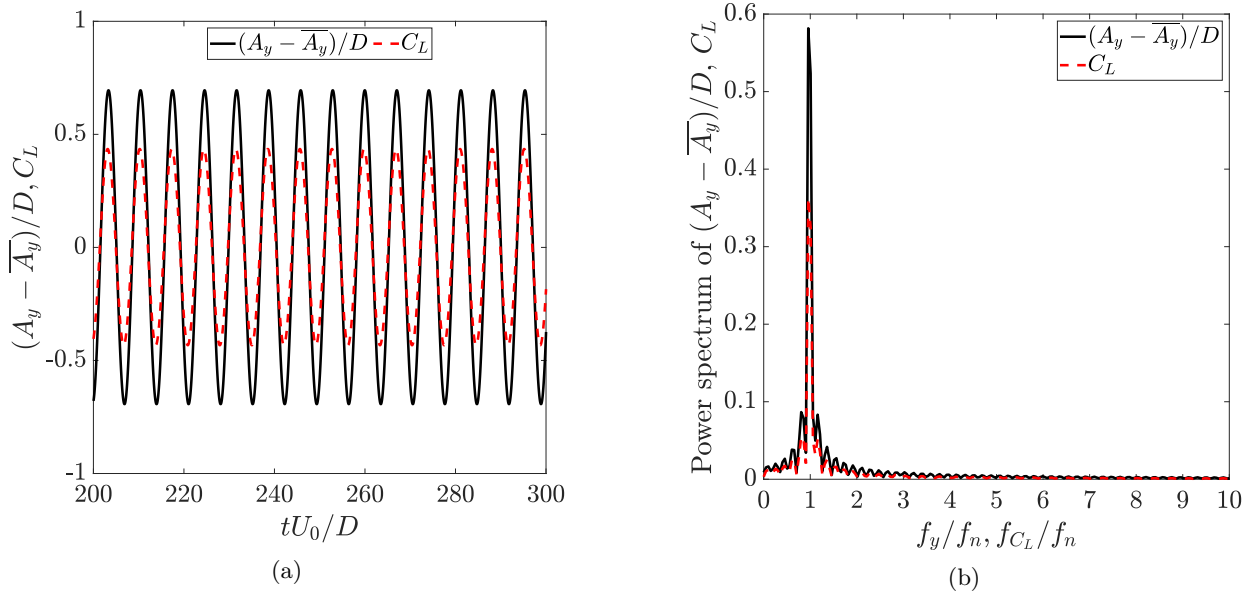


FIG. 5: (a) Variations of the dimensionless transverse vibration amplitude calculated from the mean deformed position of the cylinder $(A_y - \overline{A}_y)/D$, probed at $z/L = 1$, and lift coefficient C_L in time domain; (b) power spectra of the $(A_y - \overline{A}_y)/D$ and C_L in frequency domain. The results are gathered in the time window $tU_0/D \in [200, 300]$ at $Re = 40$, $m^* = 1$, and $U^* = 7$.

f_{C_L}/f_n are close to unity for $U^* \in [7, 9]$ and zero elsewhere. However, for $Re = 30$ and 40 , the lock-in regime is found to extend to a broader range of reduced velocities within $U^* \in [6, 13]$.

An isometric view of the cylinder undergoing large-amplitude oscillations in the lock-in regime at $Re = 40$, $m^* = 1$, and $U^* = 7$ is illustrated in Fig. 7 a. A figure-eight type motion trajectory is observed across the cylinder length. These trajectories are shown to grow in

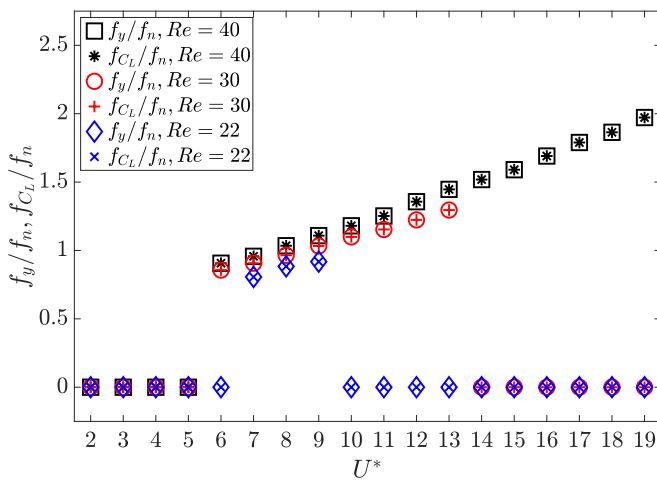


FIG. 6: Variations of the dimensionless transverse vibration frequency f_y/f_n , probed at $z/L = 1$, and lift coefficient frequency f_{C_L}/f_n with respect to U^* . The results are gathered at $m^* = 1$ for $Re = 22, 30$ and 40 .

magnitude by moving towards the tip of the cylinder. The scalograms of the dynamic response of the cylinder in the streamwise and transverse directions are given in Figs. 7 b and c, respectively. We show that the cylinder exhibits a standing wave response, with oscillations being in the first mode of vibration in both the streamwise and transverse directions.

Based on the scalograms of the cylinder response, the dimensionless frequency of the streamwise oscillations (f_x/f_n) is found to be twice that of the dimensionless frequency of the transverse vibrations (f_y/f_n), i.e., $f_x/f_n = 2f_y/f_n \approx 2$. This type of oscillatory response has been previously observed in two-degrees-of-freedom elastically mounted rigid cylinders undergoing VIVs [40]. The motion trajectory of the tip of the cylinder at $Re = 40$, and $m^* = 1$ is given in Fig. 8 for $U^* \in [6, 11]$. The figure-eight shape of the motion trajectories is associated with the frequency ratio of $f_x/f_y \approx 2$ in the lock-in regime.

B. Wake dynamics during lock-in

Here, we examine the wake dynamics in the lock-in regime for the flexible cantilever cylinder at laminar subcritical Re . A comparison between the wake of a stationary rigid cylinder at $Re = 40$, and the wake of the flexible cantilever cylinder at $z/L = 0.5$, $Re = 40$, $m^* = 1$, and $U^* = 7$ is given in Fig. 9. We show that the wake of the stationary rigid cylinder is steady and symmetric with respect to the wake centerline at $Re = 40$; however, for the flexible cantilever cylinder, the wake is unstable at

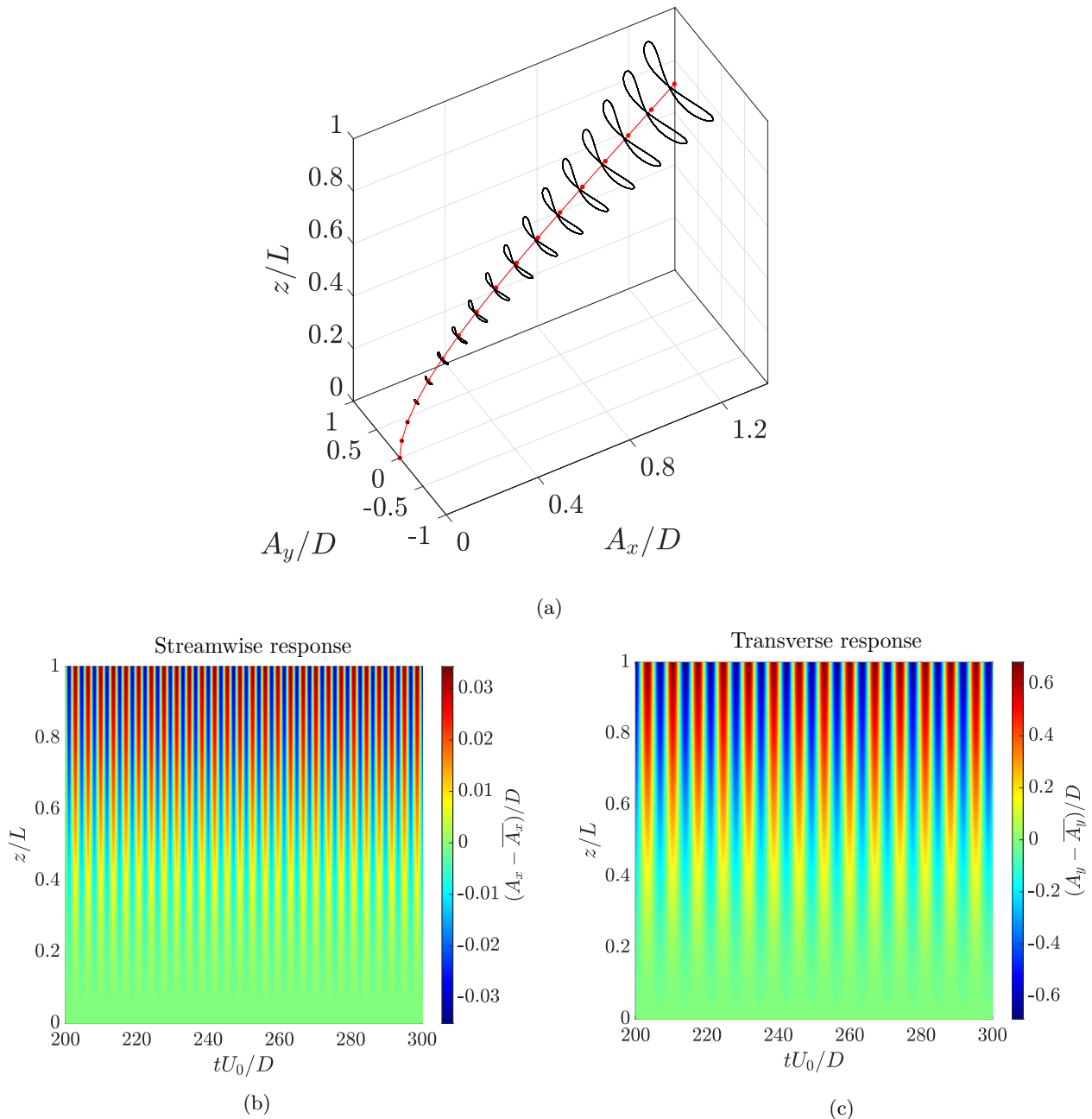


FIG. 7: (a) Motion trajectory of the flexible cantilever cylinder (illustrated by black lines); the red filled dots represent the mean position of the cylinder nodes and the red line corresponds to the cylinder's steady deflected position. (b) Scalogram of the vibrations in the streamwise direction. (c) Scalogram of the vibrations in the transverse direction. The results are gathered at $Re = 40$, $m^* = 1$, and $U^* = 7$ in the time window $tU_0/D \in [200, 300]$.

the same Re . To illustrate, we have examined the z-vorticity (ω_z) contours at different cross-sections of the flexible cantilever cylinder. As shown in Fig. 10, the wake of the cylinder is steady at $z/L = 0$ where it is connected to fixed support; however, by approaching the tip of the cylinder, the flow starts to become unstable, and peri-

odic vortex-shedding patterns are observed downstream. This finding suggests a connection between the cylinder motion and wake stability at laminar subcritical Re . To examine this conjecture, we have provided the z-vorticity iso-surfaces of the three-dimensional wake structures at $Re = 30$ and $m^* = 1$ in Fig. 11 for $U^* = 3, 6$ and 15.

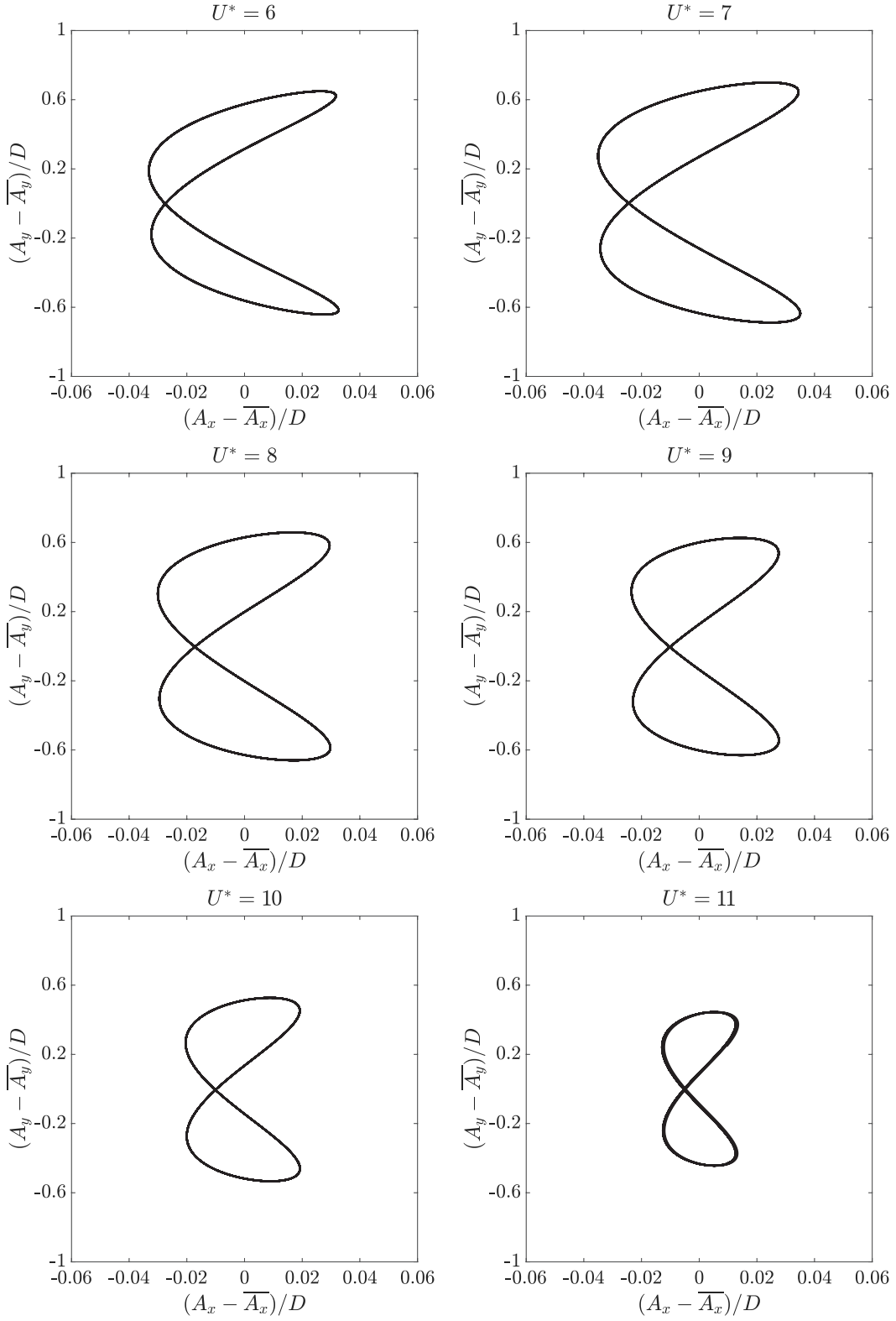


FIG. 8: Motion trajectory of the flexible cantilever cylinder at $z/L = 1$, $Re = 40$, and $m^* = 1$ for $U^* \in [6, 11]$.

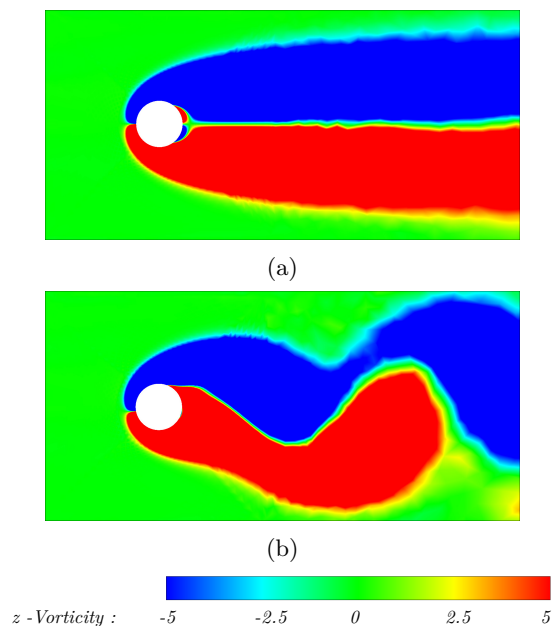


FIG. 9: Comparison of the z -vorticity contour for the (a) stationary rigid cylinder and (b) flexible cantilever cylinder at $z/L = 0.5$, $Re = 40$, $m^* = 1$, $U^* = 7$, and $tU_0/D = 200$.

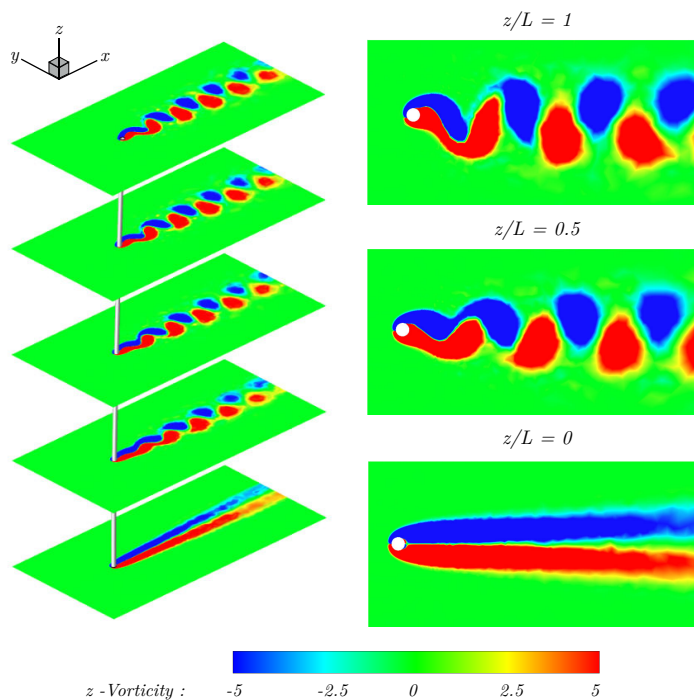


FIG. 10: Isometric view of the spanwise z -vorticity contours at various cross-sections of the flexible cantilever cylinder, with z -plane slices of the contours shown in the right-hand side for $z/L = 1$, 0.5 , and 0 .

At the given m^* and Re , $U^* = 3, 6$ and 15 represent the pre-lock-in, lock-in, and post-lock-in regimes, respectively. We find that the flow field in the wake of the flexible cantilever cylinder is steady at $U^* = 3$ (pre lock-in) and $U^* = 15$ (post lock-in); however, an unsteady wake is observed at $U^* = 6$ (see Fig. 11). The phase

diagram of the wake stability as a function of Re and U^* at $m^* = 1$ is given in Fig. 12. We find that at $Re = 20$, the flow field is steady for all U^* values; however, as Re is increased, the wake becomes unsteady for a particular range of reduced velocities. As shown in Fig. 12, the flow field in the wake of the flexible cantilever cylinder is un-

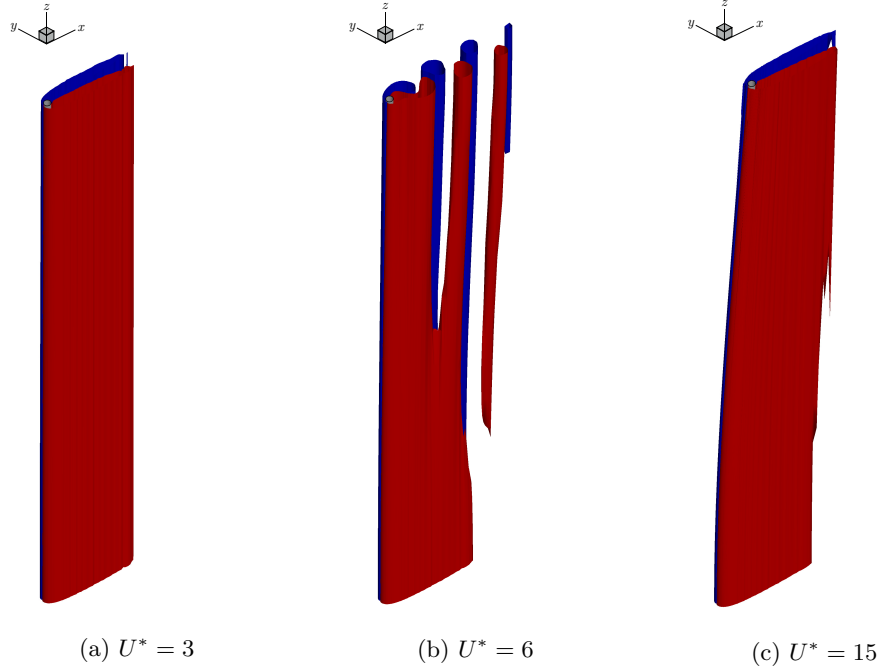


FIG. 11: Wake structures visualized by the normalized z-vorticity iso-surfaces ($\omega_z D/U_0 = -0.224, 0.224$) for the flexible cantilever cylinder at $Re = 30$, and $m^* = 1$. Red [blue] indicates regions of positive [negative] vortices.

stable at $Re = 22$ for $U^* \in [7, 9]$. The range of the wake unsteadiness is shown to become wider at higher Re . For example, this range is between $U^* \in [6, 13]$ at $Re = 30$ and increases to $U^* \in [6, 19]$ at $Re = 40$. An important point to note here is that there is a critical $U^* \in [6, 7]$ that marks the initiation of the wake unsteadiness for $22 \leq Re \leq 40$. This critical U^* also marks the lower bound of the lock-in regime, as shown in the results of Section III A. Thus, we can infer that the range of the

wake unsteadiness is closely correlated with the range of the lock-in regime at laminar subcritical Re .

We have provided the wake structures around the flexible cantilever cylinder at $Re = 40$ and $m^* = 1$ for $5 \leq U^* \leq 14$ in Fig. 13. At $U^* = 5$, which represents the pre-lock-in regime, a steady wake flow is observed behind the cylinder; however, for $U^* \geq 6$, the wake is shown to become unstable, with two alternate vortices being shed from the cylinder wake in each cycle. In addition, the wake structures close to the fixed end of the cylinder are found to be steady, regardless of U^* . As shown in Fig. 13, although an unsteady wake is observed for $U^* \geq 6$ at distances between $z/L \in [0.2, 1]$ from the fixed end of the cylinder, the wake is shown to be steady for $z/L \in [0, 0.2]$. Thus, we can deduce that the three-dimensional flow phenomena do not contribute to the wake stability at this Re regime. For the flow around an isolated cylinder, the wake has been shown to first become three-dimensional at $Re \approx 200$ [41].

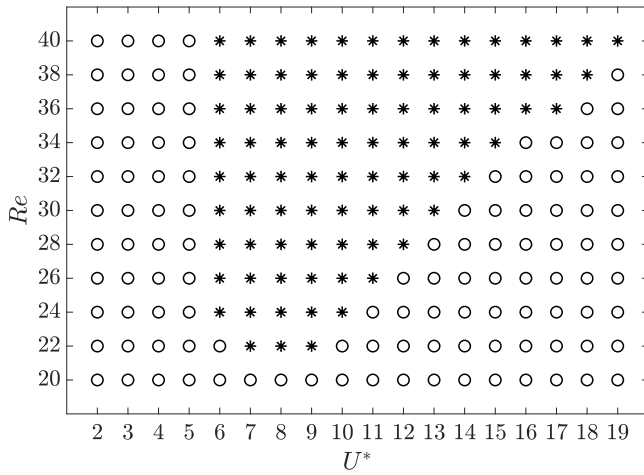


FIG. 12: Phase diagram of the wake stability as a function of Re and U^* at $m^* = 1$. Here, \circ denotes a steady wake, while $*$ represents an unsteady wake behind the flexible cantilever cylinder.

With these findings, we can deduce that the wake of a flexible cantilever cylinder could become unsteady at laminar subcritical Re , provided that two essential requirements are met: (i) the flow needs to have sufficiently large inertia to overcome the viscous damping and (ii) the system parameters need to be in the lock-in range to sustain the unsteadiness in the wake.

In the next section, we discuss the relationship between the cylinder motion and stability of the wake in detail.

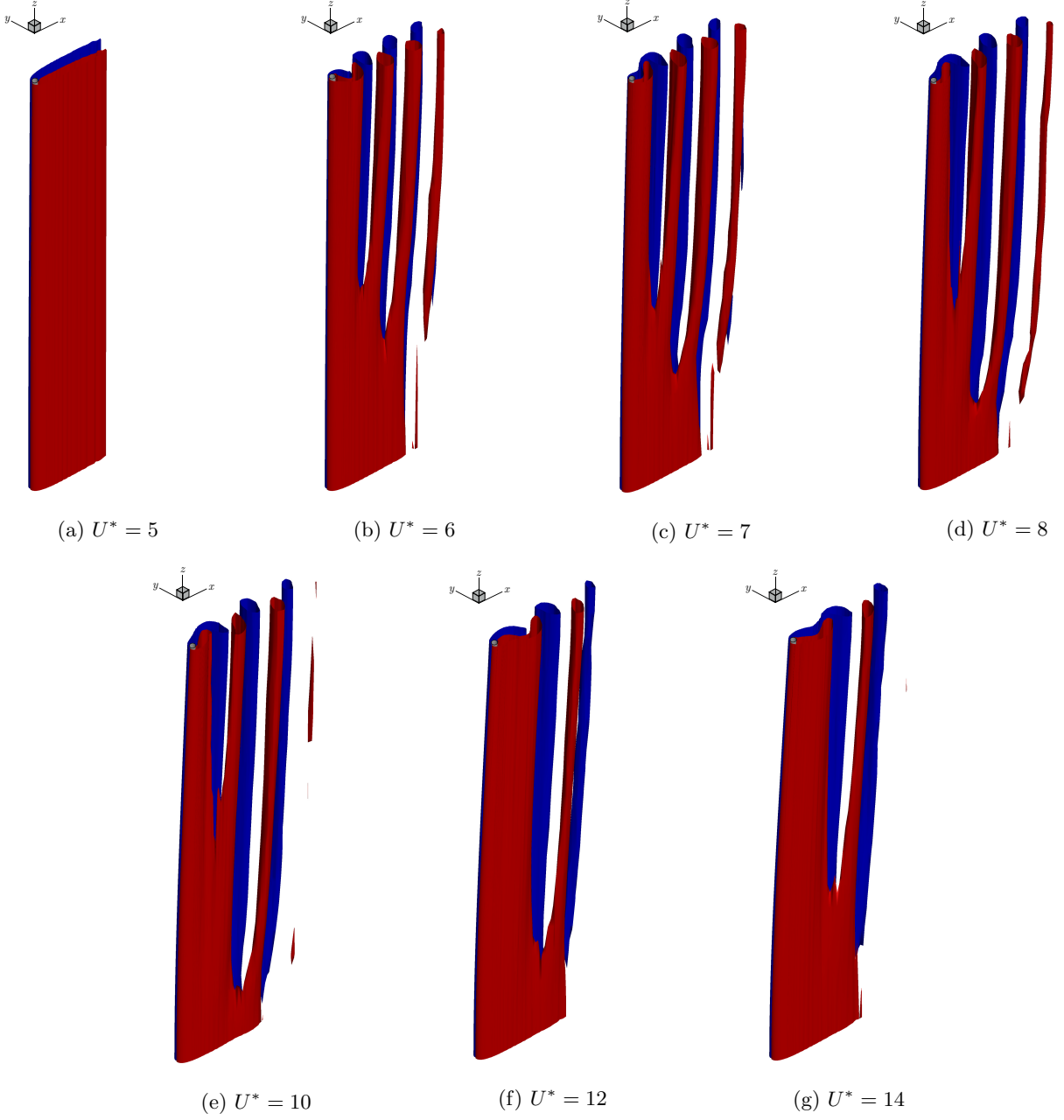


FIG. 13: Wake structures visualized by the normalized z -vorticity iso-surfaces ($\omega_z D/U_0 = -0.224, 0.224$) for the flexible cantilever cylinder at $Re = 40$, and $m^* = 1$. Red [blue] indicates regions of positive [negative] vortices.

C. Relationship between the cylinder dynamics and wake unsteadiness

Here, we pinpoint the relationship between the cylinder motion and stability of the wake at laminar subcritical Re . We recommend a combined VIV-galloping type instability as the possible cause of the wake unsteadiness for $Re < Re_{cr}$. Galloping is a velocity-dependent and damping-controlled fluid-structure instability, which is generally observed in geometrically asymmetric structures [42]. Although the flow field around an asymmetric

structure is uniform in magnitude and direction, cross-flow oscillations of the asymmetric body alter the magnitude and direction of the incident flow with respect to the body coordinate system. This change, in turn, alters the fluid forces acting on the body and could trigger the galloping instability. A deviation from symmetric cross-section in transmission lines due to ice formation [43] or in marine cables due to marine organisms [44] are some examples of the galloping instability in engineering structures. Galloping is known to cause large-amplitude sustained oscillations in flexible or elastically-mounted

structures [42].

In contrast to vortex-induced vibrations, galloping instability is induced by a relative body motion rather than the unsteady fluctuations of the flow field; hence it can occur even for steady attached flows. When the transverse force acting on a flexible or elastically-mounted body increases in the direction of motion, it adds movement to the body, and the body will displace further until the opposing stiffness or damping overcomes the movements, or the transverse force decreases when the movement is increased. For a flexible cantilever cylinder interacting with fluid flow, the body is free to deform in the streamwise and transverse directions. Although displacements in the streamwise direction do not contribute to the stability of the wake [45, 46], relative movements in the transverse direction break the wake symmetry, altering the fluid forces acting on the cylinder. This symmetry breakdown, in turn, induces a galloping-type instability by creating negative damping in the combined fluid-structure system. The low-speed galloping-type instability, together with the frequency lock-in, is most arguably the mechanism that leads to sustained unsteadiness in the wake at laminar subcritical Re .

To better understand the relationship between the cylinder motion and stability of the wake at laminar subcritical Re , we have provided the z -vorticity contours at the mid-section of the cylinder at $Re = 40$, $m^* = 1$, and $U^* = 7$ in Fig. 14. We show that the wake region behind the cylinder is steady and symmetric at $tU_0/D = 60$; however, for $tU_0/D \in [65, 75]$, relative motion of the cylinder cross-section in the transverse direction, makes the wake lose its stability and become asymmetric. This symmetry breakdown, in turn, exerts a transverse load that further increases the cylinder motion. Finally, due to the coupling between the unsteady wake and the cylinder movements, large-amplitude transverse vibrations are observed for $tU_0/D \in [80, 85]$.

In the next section, we investigate the effect of mass ratio m^* on the dynamics of the flexible cantilever cylinder and further examine the wake structures in the lock-in regime.

D. Effect of mass ratio

We first investigate the effect of mass ratio on the dynamic response of the flexible cantilever cylinder at $Re = 40$ for $U^* \in [2, 19]$. We examine the response of the cylinder at four different mass ratios, namely $m^* = 1, 10, 100$ and 1000. The results for the rms value of the dimensionless transverse vibration amplitude A_y^{rms}/D with respect to U^* are given in Fig. 15. For all the studied mass ratios, we find that the cylinder stays at its steady deflected position for $U^* \leq 5$. This steady response is present for the whole range of U^* at $m^* = 1000$. However, a discrete change in the dynamic response of the cylinder is observed for higher U^* values at $m^* = 1, 10$ and 100. We observe a sudden jump

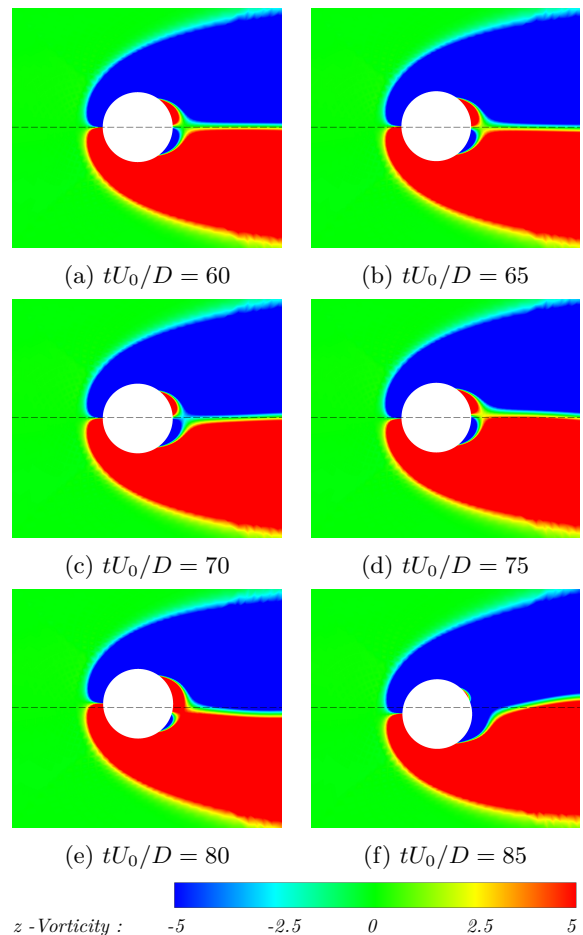


FIG. 14: Contours of z -vorticity at the cross section of the cylinder at $z/L = 0.5$, $Re = 40$, $m^* = 1$, and $U^* = 7$ in the time window $tU_0/D \in [60, 85]$.

in the amplitude response of the cylinder at $U^* = 6, 7$ and 8 at mass ratios $m^* = 1, 10$ and 100, respectively. As shown in Fig. 15, the peak of the transverse vibration amplitude is at $U^* = 7$ for $m^* = 1$ and 10, and at $U^* = 8$ for $m^* = 100$. The magnitude of the maximum A_y^{rms}/D is shown to be approximately 0.49, 0.47 and 0.39 at $m^* = 1, 10$ and 100, respectively. By further increasing the U^* , a gradual decrease in the amplitude of the transverse vibrations is observed at $m^* = 1$; however, for $m^* = 10$ and 100, there is a sharp decrease in the amplitude of the transverse vibrations for $U^* > 8$. A steady response is observed for $U^* \geq 11$ at $m^* = 10$ and for $U^* \geq 10$ at $m^* = 100$.

Fig. 16 shows the frequency response of the fluid-structure system in terms of the dimensionless transverse vibration frequency f_y/f_n and the dimensionless lift coefficient frequency f_{CL}/f_n at $Re = 40$ for $m^* = 1, 10$ and 100 with respect to U^* . We show that for all three mass ratios, there is a frequency match between the frequency of the transverse vibrations f_y , frequency of the lift coefficient f_{CL} , and the first-mode natural frequency of the cylinder f_n for a specific range of U^* . This range

is within $U^* \in [8, 9]$ at $m^* = 100$ and within $U^* \in [7, 10]$ at $m^* = 10$. At $m^* = 1$, the lock-in regime begins at $U^* = 6$, however, the beam is shown to oscillate in frequencies higher than its first-mode natural frequency at larger U^* values.

Based on our findings, we observe that by increasing m^* , the range of the lock-in regime becomes narrower. This behavior is because of stronger inertial coupling and added mass effects at lower mass ratios. It should be noted that for Reynolds numbers beyond $Re_{cr} \approx 45$, interactions between the unsteady wake and the cylinder motion could lead to sustained vibrations for mass ratios of $O(100 - 1000)$, which are not examined in our current work.

A qualitative representation of the cylinder motion trajectory at $z/L = 1$ and $Re = 40$ with respect to U^* is given in Fig. 17 for $m^* = 1, 10$, and 100. We show that as m^* is increased, the motion trajectory of the cylinder in the lock-in regime shifts from a figure-eight type response at $m^* = 1$ to a dominated motion in the transverse direction at $m^* = 100$.

To examine the wake structures in the lock-in regime at different mass ratios, we have provided the z-vorticity iso-surfaces around the cylinder at $Re = 40$ and $U^* = 8$ for $m^* = 1, 10$ and 100 in Fig. 18. We observe that for all three m^* , two alternate vortices are shed from the cylinder wake in each cycle. This finding suggests that at a fixed Re , the vortex shedding patterns in the wake of the flexible cantilever cylinder are independent of the mass ratio m^* .

Finally, we connect our findings to the dynamic response of rat and seal whiskers in fluid flow. The presented results in this section for $m^* = 1$ and 100 are qualitative representatives of a seal and a rat whisker in fluid flow, respectively. As mentioned in Section I, the interaction of a rat's whisker with low-speed airflow occurs at $Re < 50$. Based on our results for the flexible can-

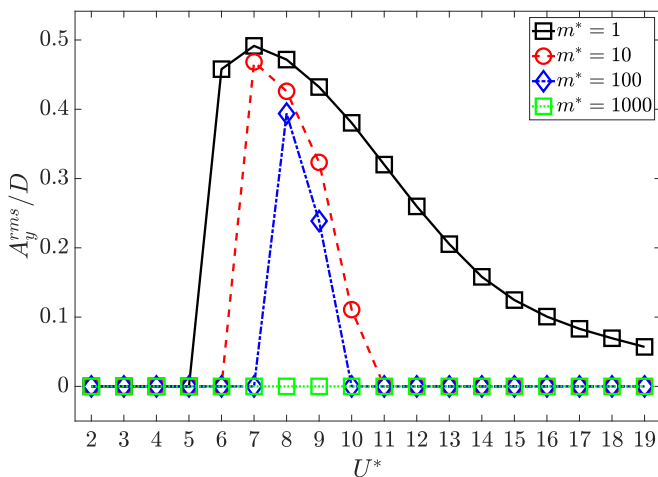


FIG. 15: Root-mean-square value of the dimensionless transverse vibration amplitude A_y^{rms}/D at $z/L = 1$ as a function of U^* at $Re = 40$ for $m^* = 1, 10, 100$ and 1000.

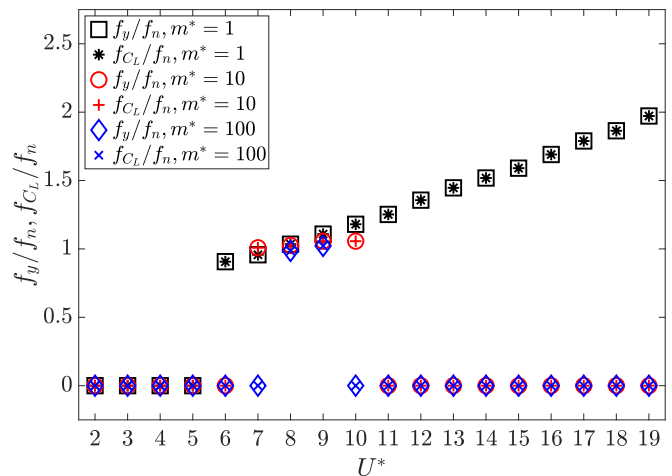


FIG. 16: Variations of the dimensionless transverse vibration frequency f_y/f_n , probed at $z/L = 1$, and lift coefficient frequency f_{CL}/f_n with respect to U^* . The results are gathered at $Re = 40$ for $m^* = 1, 10$ and 100.

tiler cylinder, a rat's whisker at laminar subcritical Re is expected to experience a VIV-galloping type instability in the lock-in regime. In addition, flutter instability at reduced velocities of $O(100)$ could appear in a rat's whisker, which requires further investigations.

For the case of a seal whisker in water flow, we characterize the oscillations as a VIV-dominant mechanism that occurs due to interactions between the whisker and unsteady wake at $Re \approx 1000$. Our results for the dynamic response of the flexible cantilever cylinder at $m^* = 1$ could be used to interpret the response of a seal whisker in low-speed laminar water flows.

Based on the available data in the literature regarding the amplitude response of an elastically mounted rigid cylinder at laminar Re [15], we can deduce that the amplitude response of the flexible cantilever cylinder at $Re \approx 1000$ would be slightly higher than the values presented in our current work. In addition, the vibration amplitude of a seal whisker is predicted to be significantly lower than the vibration amplitude of the flexible cantilever cylinder under similar conditions. Based on the experiments by Refs [33, 47], lower amplitudes in a seal whisker, compared to the flexible cantilever cylinder, are due to the seal whisker's undulated geometry that helps reduce the fluid forces during VIVs.

IV. CONCLUSIONS

In this paper, we have investigated the fluid-structure interaction of a flexible cantilever cylinder at laminar subcritical Re . Through numerical simulations, we assessed the dynamic response of the cylinder as a function of reduced velocity U^* , for Reynolds numbers between $20 \leq Re \leq 40$ and mass ratios between $1 \leq m^* \leq 1000$. We found that for $Re = 20$, the flexible cantilever cylin-

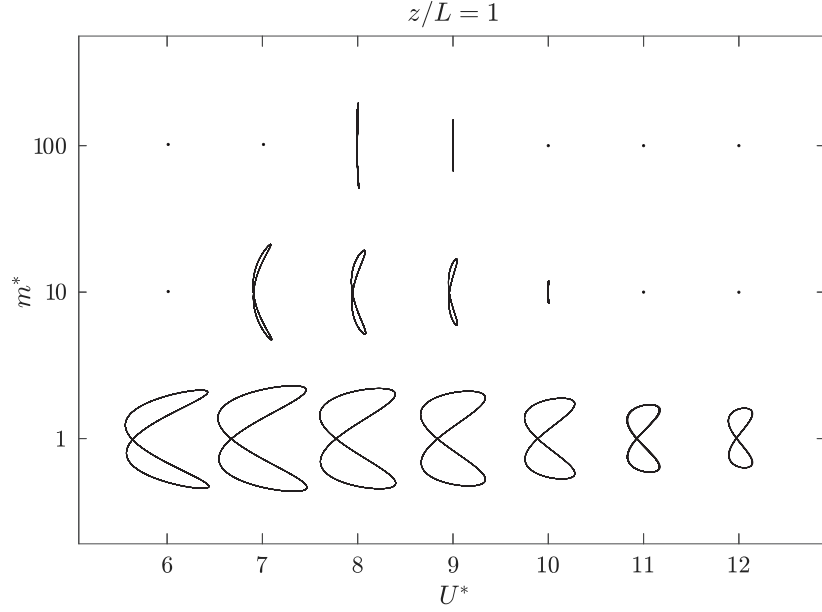


FIG. 17: A representation of the motion trajectory of the flexible cantilever cylinder with respect to U^* at $z/L = 1$ and $Re = 40$ for $m^* = 1, 10$ and 100 . The filled dot (.) represents a steady response.

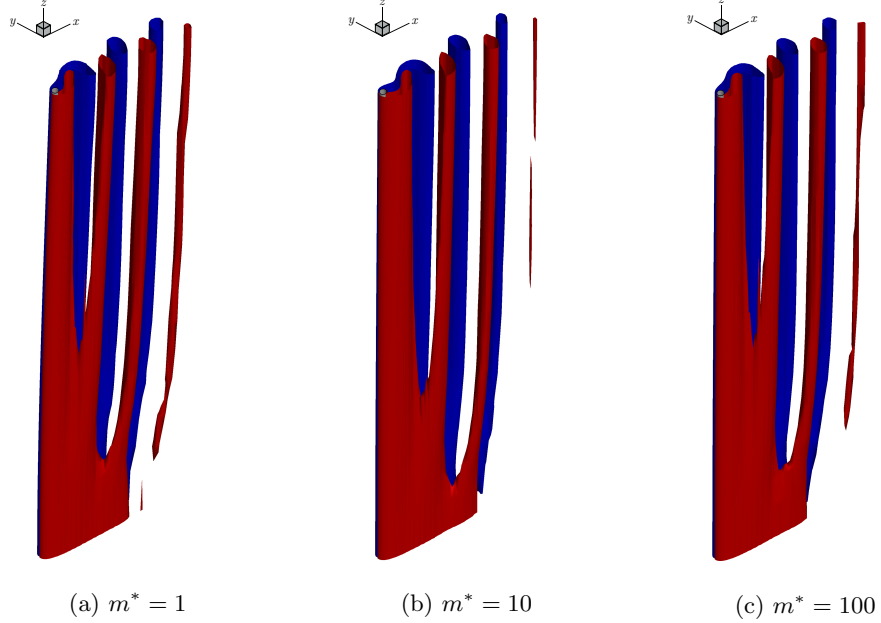


FIG. 18: Wake structures visualized by the normalized z-vorticity iso-surfaces ($\omega_z D/U_0 = -0.224, 0.224$) for the flexible cantilever cylinder at $Re = 40$, and $U^* = 8$. Red [blue] indicates regions of positive [negative] vortices.

der remains in its steady deflected position for the whole range of studied U^* and m^* . However, for $22 \leq Re \leq 40$, we observed that the cylinder experiences sustained oscillations when certain conditions are satisfied. We showed that the frequency of the transverse vibrations matches the frequency of the periodic lift force during the oscillations. Also, these two frequencies were found to be approximately equal to the first-mode natural frequency

of the cylinder for a particular range of U^* . This specific range, known as the lock-in regime, was shown to strongly depend on the Reynolds number Re and mass ratio m^* ; we found that at laminar subcritical Re , the range of the lock-in regime decreases by increasing m^* , whereas this range was shown to increase by increasing Re . Finally, we identified two requirements for the wake unsteadiness at laminar subcritical Re : (i) the flow needs

to have sufficiently large inertia to overcome the viscous damping, and (ii) the system parameters need to be in the lock-in range. When these two conditions are satisfied, the cylinder experiences a combined VIV-galloping type instability. This instability was shown to break the symmetry of the wake and lead to sustained large-amplitude vibrations and unsteadiness in the wake at laminar subcritical Re . We anticipate that the presented systematic analysis can help improve our understanding of the lock-in mechanism in flexible cantilever structures. Further research is required towards a parametric investigation of the dynamic response of the cylinder at high reduced velocities of $O(100)$, where potential flutter-type instabilities could be present. In addition, the effects of structural nonlinearities should be accounted from a practical viewpoint for different flow incidence with a

broader range of Re and U^* to fully understand the dynamic instabilities of the coupled system.

ACKNOWLEDGMENTS

The authors would like to acknowledge the Natural Sciences and Engineering Research Council of Canada (NSERC) for the funding. This research was enabled in part through computational resources and services provided by WestGrid (<https://westgrid.ca/>), Compute Canada (<https://computecanada.ca/>), and the Advanced Research Computing facility at the University of British Columbia (<https://arc.ubc.ca/>).

-
- [1] Y. Z. Law and R. K. Jaiman, Wake stabilization mechanism of low-drag suppression devices for vortex-induced vibration, *Journal of Fluids and Structures* **70**, 428 (2017).
- [2] A. Chizfahm and R. Jaiman, Data-driven stability analysis and near-wake jet control for the vortex-induced vibration of a sphere, *Physics of Fluids* **33**, 044104 (2021).
- [3] S. Dong, G. S. Triantafyllou, and G. E. Karniadakis, Elimination of vortex streets in bluff-body flows, *Phys. Rev. Lett.* **100**, 204501 (2008).
- [4] Y. Xia, S. Michelin, and O. Doaré, Fluid-solid-electric lock-in of energy-harvesting piezoelectric flags, *Phys. Rev. Applied* **3**, 014009 (2015).
- [5] A. Chizfahm, E. A. Yazdi, and M. Eghtesad, Dynamic modeling of vortex induced vibration wind turbines, *Renewable Energy* **121**, 632 (2018).
- [6] W. B. Hobbs and D. L. Hu, Tree-inspired piezoelectric energy harvesting, *Journal of Fluids and Structures* **28**, 103 (2012).
- [7] Y. J. Lee, Y. Qi, G. Zhou, and K. B. Lua, Vortex-induced vibration wind energy harvesting by piezoelectric mems device in formation, *Scientific Reports* **9**, 1 (2019).
- [8] P. S. Gurugubelli and R. K. Jaiman, Self-induced flapping dynamics of a flexible inverted foil in a uniform flow, *Journal of Fluid Mechanics* **781**, 657 (2015).
- [9] J. Z. Gul, K. Y. Su, and K. H. Choi, Fully 3D Printed Multi-Material Soft Bio-Inspired Whisker Sensor for Underwater-Induced Vortex Detection, *Soft Robotics* **5**, 122 (2018).
- [10] M. Scharff, P. Schorr, T. Becker, C. Resagk, J. H. Miranda, and C. Behn, An artificial vibrissa-like sensor for detection of flows, *Sensors (Switzerland)* **19**, 1 (2019).
- [11] R. D. Blevins, *Flow-induced vibration* (Van Nostrand Reinhold, New York, 1990).
- [12] A. Khalak and C. H. K. Williamson, Motions, forces and mode transitions in vortex-induced vibrations at low mass-damping, *Journal of Fluids and Structures* **13**, 813 (1999).
- [13] T. Sarpkaya, Vortex-Induced Oscillations: A Selective Review, *Journal of Applied Mechanics* **46**, 241 (1979).
- [14] C. H. K. Williamson and R. Govardhan, Vortex-induced vibrations, *Annual Review of Fluid Mechanics* **36**, 413 (2004).
- [15] P. W. Bearman, Circular cylinder wakes and vortex-induced vibrations, *Journal of Fluids and Structures* **27**, 648 (2011).
- [16] N. Jauvtis and C. H. K. Williamson, The effect of two degrees of freedom on vortex-induced vibration at low mass and damping, *Journal of Fluid Mechanics* **509**, 23–62 (2004).
- [17] R. N. Govardhan and C. H. K. Williamson, Defining the ‘modified griffin plot’ in vortex-induced vibration: revealing the effect of reynolds number using controlled damping, *Journal of Fluid Mechanics* **561**, 147–180 (2006).
- [18] C. H. Williamson and R. Govardhan, A brief review of recent results in vortex-induced vibrations, *Journal of Wind Engineering and Industrial Aerodynamics* **96**, 713 (2008).
- [19] T. Sarpkaya, A critical review of the intrinsic nature of vortex-induced vibrations, *Journal of Fluids and Structures* **19**, 389 (2004).
- [20] R. H. J. Willden and J. M. R. Graham, Bluff body wakes and vortex-induced vibrations multi-modal vortex-induced vibrations of a vertical riser pipe subject to a uniform current profile, *European Journal of Mechanics - B/Fluids* **23**, 209 (2004).
- [21] A. D. Trim, H. Braaten, H. Lie, and M. Tognarelli, Experimental investigation of vortex-induced vibration of long marine risers, *Journal of Fluids and Structures* **21**, 335 (2005).
- [22] J. K. Vandiver, V. Jaiswal, and V. Jhingran, Insights on vortex-induced, traveling waves on long risers, *Journal of Fluids and Structures* **25**, 641 (2009).
- [23] R. Bourguet, G. E. Karniadakis, and M. S. Triantafyllou, Vortex-induced vibrations of a long flexible cylinder in shear flow, *Journal of Fluid Mechanics* **677**, 342 (2011).
- [24] V. Joshi and R. K. Jaiman, A variationally bounded scheme for delayed detached eddy simulation: Application to vortex-induced vibration of offshore riser, *Computers and Fluids* **157**, 84 (2017).
- [25] G. R. Franzini, C. P. Pesce, R. T. Gonçalves, A. L. C. Fajarra, and P. Mendes, An experimental investigation on concomitant Vortex-Induced Vibration and axial top-motion excitation with a long flexible cylinder in vertical

- configuration, *Ocean Engineering* **156**, 596 (2018).
- [26] G. Baarholm, C. Larsen, and H. Lie, On fatigue damage accumulation from in-line and cross-flow vortex-induced vibrations on risers, *Journal of Fluids and Structures* **22**, 109 (2006).
- [27] J. R. Chaplin, P. W. Bearman, F. J. Huera Huarte, and R. J. Pattenden, Laboratory measurements of vortex-induced vibrations of a vertical tension riser in a stepped current, *Journal of Fluids and Structures* **21**, 3 (2005).
- [28] J. K. Shang, H. A. Stone, and A. J. Smits, Vortex and structural dynamics of a flexible cylinder in cross-flow, *Physics of Fluids* **26**, 10.1063/1.4878341 (2014).
- [29] Y. S. W. Yu, N. E. Bush, and M. J. Z. Hartmann, Whisker vibrations and the activity of trigeminal primary afferents in response to airflow, *The Journal of Neuroscience* **39**, 5881–5896 (2019).
- [30] Y. S. W. Yu, M. M. Graff, and M. J. Z. Hartmann, Mechanical responses of rat vibrissae to airflow, *Journal of Experimental Biology* **219**, 937 (2016).
- [31] Y. S. W. Yu, M. M. Graff, C. S. Bresee, Y. B. Man, and M. J. Z. Hartmann, Whiskers aid anemotaxis in rats, *Science Advances* **2**, 10.1126/sciadv.1600716 (2016).
- [32] G. Dehnhardt, B. Mauck, W. Hanke, and H. Bleckmann, Hydrodynamic trail-following in harbor seals (*phoca vitulina*), *Science* **293**, 102 (2001).
- [33] H. R. Beem and M. Triantafyllou, Wake-induced 'slaloming' response explains exquisite sensitivity of seal whisker-like sensors, *Journal of Fluid Mechanics* **783**, 306 (2015).
- [34] D. Park and K. S. Yang, Flow instabilities in the wake of a rounded square cylinder, *Journal of Fluid Mechanics* **793**, 915 (2016).
- [35] W. Yao and R. K. Jaiman, Model reduction and mechanism for the vortex-induced vibrations of bluff bodies, *Journal of Fluid Mechanics* **827**, 357 (2017).
- [36] T. J. R. Hughes, W. K. Liu, and T. K. Zimmermann, Lagrangian-Eulerian finite element formulation for incompressible viscous flows, *Computer Methods in Applied Mechanics and Engineering* **29**, 329 (1981).
- [37] R. D. Blevins, *Formulas for dynamics, acoustics and vibration* (Wiley, 2016).
- [38] R. K. Jaiman, M. Z. Guan, and T. P. Miyanawala, Partitioned iterative and dynamic subgrid-scale methods for freely vibrating square-section structures at subcritical Reynolds number, *Computers and Fluids* **133**, 68 (2016).
- [39] R. K. Jaiman, N. R. Pillalamarri, and M. Z. Guan, A stable second-order partitioned iterative scheme for freely vibrating low-mass bluff bodies in a uniform flow, *Computer Methods in Applied Mechanics and Engineering* **301**, 187 (2016).
- [40] Z. Li, W. Yao, K. Yang, R. K. Jaiman, and B. C. Khoo, On the vortex-induced oscillations of a freely vibrating cylinder in the vicinity of a stationary plane wall, *Journal of Fluids and Structures* **65**, 495 (2016).
- [41] G. E. Karniadakis and G. S. Triantafyllou, Three-dimensional dynamics and transition to turbulence in the wake of bluff objects, *Journal of Fluid Mechanics* **238**, 1–30 (1992).
- [42] D. J. P. Hartog, *Mechanical Vibrations* (Dover Publications, 1985).
- [43] M. Farzaneh, *Atmospheric Icing of Power Networks*, Vol. 84 (Springer, 2008).
- [44] A. Simpson, Determination of the natural frequencies of multiconductor overhead transmission lines, *Journal of Sound and Vibration* **20**, 417 (1972).
- [45] S. Tang and N. Aubry, On the symmetry breaking instability leading to vortex shedding, *Physics of Fluids* **9**, 2550 (1997).
- [46] G. L. Vasconcelos, M. N. Moura, and A. M. J. Schakel, Vortex motion around a circular cylinder, *Physics of Fluids* **23**, 123601 (2011).
- [47] W. Hanke, M. Witte, L. Miersch, M. Brede, J. Oeffnet, M. Michael, F. Hanke, A. Leder, and G. Dehnhardt, Harbor seal vibrissa morphology suppresses vortex-induced vibrations, *Journal of Experimental Biology* **213**, 2665 (2010).